Manuscript prepared for The Cryosphere
with version 2015/04/24 7.83 Copernicus papers of the LaTeX class copernicus.cls.
Date: 26 January 2016

Late summer sea ice segmentation with multi-polarisation SAR features in C- and X-band

A. S. Fors[1], C. Brekke[1], A. P. Doulgeris[1], T. Eltoft[1], A. H. H. Renner[2], and S. Gerland[3]

[1]Department of Physics and Technology, University of Tromsø – The Arctic University of Norway, 9037 Tromsø, Norway
[2]Institute of Marine Research, 9294 Tromsø, Norway
[3]Norwegian Polar Institute, FRAM Centre, 9296 Tromsø, Norway

Correspondence to: A. S. Fors (ane.s.fors@uit.no)

Abstract. In this study, we investigate the potential of sea ice segmentation by C- and X-band multi-polarisation synthetic aperture radar (SAR) features during late summer. Five high-resolution satellite SAR scenes were recorded in the Fram Strait covering iceberg-fast first-year and old sea ice during a week with air temperatures varying around zero degrees Celsius. Sea ice thickness, surface roughness and aerial photographs were collected during a helicopter flight at the site. Six polarimetric SAR features were extracted for each of the scenes. The ability of the individual SAR features to discriminate between sea ice types and their temporal consistency were examined. All SAR features were found to add value to sea ice type discrimination. Relative kurtosis, geometric brightness, cross-polarisation ratio and co-polarisation correlation angle were found to be temporally consistent in the investigated period, while co-polarisation ratio and co-polarisation correlation magnitude were found to be temporally inconsistent. An automatic feature-based segmentation algorithm was tested both for a full SAR feature set, and for a reduced SAR feature set limited to temporally consistent features. In C-band, the algorithm produced a good late summer sea ice segmentation, separating the scenes into segments that could be associated with different sea ice types in the next step. The X-band performance was slightly poorer. Excluding temporally inconsistent SAR features improved the segmentation in one of the X-band scenes.

1 Introduction

A decline in the Arctic sea ice extent has been observed during the last decades, together with a large reduction in sea ice thickness and sea ice volume (Kwok et al., 2009a; Parkinson and Comiso, 2013; Laxon et al., 2013; Meier et al., 2014). At the same time, the melt season has lengthened at a rate of about five days per decade since 1979 (Stroeve et al., 2014). To understand the processes governing these changes, and to meet the needs of shipping, oil and gas industries in an increasingly accessible

Arctic, more detailed mapping and monitoring of the summer sea ice cover are required (Stephenson et al., 2013).

Synthetic aperture radar (SAR) is widely used in operational sea ice monitoring. The Canadian Ice Service alone processes ten to twelve thousand SAR images every year (Moen et al., 2013). Operating in the microwave frequency, SAR has the advantage of providing all-weather and day-and-night imagery. At present, operational sea ice services use single and dual polarimetric SAR images (HH + HV or VH + VV) in sea ice monitoring due to their wide swath widths and good temporal coverage. However, on a local scale, more information and improved sea ice segmentation can be retrieved from full polarimetric SAR imagery (HH + HV + VH + VV). Today, such data is in limited use mainly due to its reduced coverage. The recent development of compact polarimetry could open the way for more polarimetric radar information to be retrieved at larger swath widths (Raney, 2007; Dabboor and Geldsetzer, 2014).

C-band (5.4 GHz) is considered the preferred frequency in operational sea ice satellite monitoring, offering good all-season capability (Onstott, 1992). With the launch of TerraSAR-X (2007) and COSMO Skymed (2007) new opportunities to investigate the potential use of X-band (frequency of 9,6 GHz) in sea ice satellite monitoring appeared. Several studies have investigated the application of X-band radar for sea ice mapping through ground based, airborne and satellite borne platforms. X-band is found to have good separation capabilities between first-year ice and old ice (Onstott, 1992), between water and sea ice (Brath et al., 2013), and in detection of thin ice (Matsuoka et al., 2001). Results from the Baltic Sea suggest that the information content in C- and X-band are largely equivalent (Mäkynen and Hallikainen, 2004; Eriksson et al., 2010), while X-band was found to add information when used in combination with C-band in the Arctic Ocean (Brath et al., 2013).

Several techniques for automatic segmentation of sea ice in SAR scenes exist. Methods consist of gamma distribution mixture models, thresholding of polarimetric features, K-means clustering, neural networks, Markov random field models, Gaussian mixture models, Wishart classifiers, and iterative region growing using sematics (see Moen et al., 2013, and references therein). Several of these methods are feature-based methods, making use of a feature set in the segmentation. They have the advantage of being flexible as the input features used can be varied with, e.g., location and seasonal conditions, and the features offer possible post-segmentation information as an interpretation and labeling source. Moen et al. (2013) showed promising results in segmenting a full polarimetric sea ice scene taken under winter conditions (low temperatures and snow cover) with a simple feature-based multi-channel SAR segmentation method described in Doulgeris and Eltoft (2010) and Doulgeris (2013), utilising six polarimetric features derived from the covariance matrix.

Research has been conducted on SAR and microwave scatterometer measurements of sea ice since the early 1990s (Onstott, 1992). Most of the conducted studies have been in winter and late fall, and the number of studies in the melt period is limited. In winter, differences in salinity content and degree of deformation of sea ice make it possible to separate multiyear ice (MYI) and different stages

of first-year ice (FYI) from each other. During summer, smaller differences in salinity between MYI and FYI and the presence of moist snow on the sea ice surface make monitoring with SAR challenging. SAR is sensitive to the large changes in relative permittivity connected to air temperatures close to 0°C (Vant, 1974; Barber et al., 1998), and to variation in moisture content in the sea ice volume caused by freeze and melt cycles (Scharien et al., 2010). Early studies on the use of SAR and microwave scatterometer data for summer sea ice applications can be found in, e.g., Onstott (1992), Gogineni et al. (1992), Carlstrom and Ulander (1993), Jeffries et al. (1997), and Yackel and Barber (2000). Newer studies include examination of backscatter signatures of multiyear sea ice with ship-based scatterometer (Isleifson et al., 2009) and investigation of the use of a supplementary frequency of either X- or Ku-band in addition to C-band in late summer sea ice classification with an airborne scatterometer (Brath et al., 2013). Satellite-based studies include separation of MYI and FYI by dual polarisation intensity data from Radarsat-2 (Warner et al., 2013), classification potential of polarimetric features from Radarsat-2 (Gill et al., 2013) and investigations of melt pond fraction retrieval from co-polarisation ratio data acquired by Radarsat-2 (Scharien et al., 2012, 2014b). Separating different sea ice types during summer-melt is still a challenge.

The objective of this study is to investigate the potential of sea ice segmentation using C- and X-band multi-polarisation SAR features during late summer. A dataset consisting of five high-resolution C- and X-band scenes recorded on iceberg-fast first-year and old ice in the Fram Strait in August and September 2011 is employed in our study. The satellite data is combined with airborne measurements from a helicopter flight at the site. We explore how the features and feature-based automatic segmentation successfully employed on FYI during winter conditions in Moen et al. (2013) perform on late summer sea ice with air temperatures close to 0°C. Our study consists of two parts: Firstly, the suitability of the individual features for use in late summer sea ice segmentation is evaluated. This is done by investigating the ability of the individual features to discriminate between sea ice types and their temporal consistency during changing temperature conditions. A reduced set of the four most temporally consistent features is suggested for use in segmentation. Secondly, a feature-based automatic segmentation algorithm is tested on the dataset. We investigate whether it groups the scenes into reasonable segments, which are possible to associate with distinct sea ice types. The algorithm is tested both with a full feature set, and with the reduced feature set suggested in the first part of the study. The segmented images are evaluated both visually, and by pixel-wise evaluation of regions with known geophysical properties.

2 Methods

In this study, we examine the potential of six polarimetric SAR features for use in late summer sea ice segmentation. To simplify the study, five regions of interest (ROIs) with different sea ice types were defined based on information from the satellite scenes and the helicopter flight at the site. The

first part of this section describes the dataset utilized in our study. In the second part we explain the design of the study, including the choice of ROIs, the generation of polarimetric SAR features and the methodology of the analysis.

2.1 Study site

Fram Strait is a dynamic region characterised by the outflow of sea ice from the central Arctic Ocean (e.g. Kwok, 2009b; Renner et al., 2014). The sea ice cover is therefore highly variable with both FYI and MYI, and contains a large fraction of deformed ice. In late summer, the snow cover has usually melted completely, leading to melt ponds on top of the ice (e.g. Renner et al., 2013). While in most parts of Fram Strait, southward drift leads to fast movement of the sea ice, a region with iceberg-fast ice forms in some years in western Fram Strait (Hughes et al., 2011). In this region, the ice cover varies between rough ice due to deformation and very level ice where the ice is formed during winter and protected from impact (Beckers et al., 2015; unpublished data). The study site was situated in this area (Fig. 1). Both FYI and old sea ice in different stages of development were represented at the site.

2.2 Dataset

The data used in this study were collected from ship, helicopter and satellite platforms during a coordinated campaign in Fram Strait in late summer 2011. The dataset consists of several high resolution multi-polarimetric SAR scenes, together with airborne observations collected from a helicopter (Table 1). In addition, meteorological observations from the scientific vessel R/V *Lance* provided information about the changing weather conditions during the campaign. The area covered by the satellite scenes could not be reached by the ship, and the helicopter did not have the opportunity to land within the area, therefore no in situ measurements from the sea ice surface were retrieved.

2.2.1 Satellite measurements

For this study, three quad polarimetric C-band scenes from the Canadian Radarsat-2 (RS-2) satellite (denoted R1, R2 and R3) and two dual polarimetric X-band scenes from the German TerraSAR-X (TS-X) satellite (denoted T1 and T2) were used. More details about the scenes can be found in Table 1, and the positions of the scenes are displayed in Fig. 1. All scenes were acquired during ascending orbits. The RS-2 scenes have a coverage of $25\,\mathrm{km}$ (range) $\times$ $25\,\mathrm{km}$ (azimuth), while the TS-X scenes have a coverage of $15\,\mathrm{km}$ (range) $\times$ $50\,\mathrm{km}$ (azimuth).

2.2.2 Airborne measurements

Airborne measurements were conducted during a helicopter flight out from R/V *Lance* within the period of the satellite campaign (see Table 1). They include sea ice thickness, relative surface rough-

ness and aerial images. The track of the flight is displayed together with the location of the satellite scenes in Fig. 1.

Measurements of total snow plus sea ice thickness (from now on referred to as sea ice thickness) were performed with an electromagnetic induction sounder (EM-bird), which was towed underneath the helicopter and flown at a height of about $15\,\mathrm{m}$ above the surface. More details about the EM-bird can be found in Haas et al. (2009) and Renner et al. (2013, 2014). From this device, the difference in conductivity between sea ice and water is used to find the height of the EM-bird above the ice/water interface, and a laser altimeter integrated in the EM-bird detects the distance between the EM-bird and the snow/ice surface. The difference between the two measures gives the sea ice thickness. The footprint of the EM-bird has a diameter of about $50\,\mathrm{m}$ (depending on the height of the instrument). At the time of the acquisition there was very little or no snow on top of the sea ice, confirmed by the aerial photos and observations from scientists onboard the helicopter.

The data from the laser altimeter mounted on the EM-bird can be used to extract surface roughness (von Saldern et al., 2006; Beckers et al., 2015). Calibration is needed to remove helicopter altitude variations. This was done by the three-step high- and low-pass filtering method described in Hibler (1972). The resulting surface elevation profiles are relative to the level ice. Surface roughness is in this study presented as the standard deviation of the profile surface elevation about the mean (root mean square height), R_q,

$$R_q = \sqrt{\frac{1}{N}\sum_{i=1}^{N}(y_i - \overline{y})^2}, \tag{1}$$

where N represents the number of measurements, $\overline{y}$ the mean height above level ice, and y_i the height above level ice of sample i. Each ROI profile is $400\,\mathrm{m}$ long, and N varies between 960 and 1067, depending on the speed of the helicopter.

The helicopter was equipped with a digital camera (GoPro YHDC5170, focal length $5\,\mathrm{mm}$, view angle $127°$), taking downward looking photographs of the sea ice surface. The area covered by each image was about $85\,\mathrm{m}$ (length) $\times$ $110\,\mathrm{m}$ (width) and the sampling rate was $0.5\,\mathrm{Hz}$. The images were processed with a semi-automatic classification algorithm, separating classes of open water, submerged ice, melt ponds, very thin ice and thicker ice, as described inRenner et al. (2013). In an accuracy assessment of the method performed in Renner et al. (2013), 76% of the melt pond pixels were correctly classified. The melt pond fraction, i.e., the percentage coverage of melt ponds retrieved from each image, is used in our description of the sea ice types. No additional ground information could be retrieved about the state of the melt ponds at the site of the satellite scenes during the campaign; hence, we do not know whether the melt ponds were open or refrozen at the time of the acquisitions. According to the cruise report, open melt ponds were observed during the first days of the cruise, but from 26 August, a major part of the melt ponds had started to freeze over. Melt pond measurements in open melt ponds at the ice edge were however performed until 31 August.

2.2.3 Meteorological information

SAR scattering properties of sea ice are highly affected by temperature and humidity, and meteorological information can therefore aid the interpretation of SAR satellite scenes. Meteorological measurements were performed on R/V *Lance* during the campaign (Fig. 2). An automatic weather station at R/V Lance consisting of an air temperature sensor (3455), an air pressure sensor (2810) and a relative humidity sensor (3445), all from Aanderaa (numbers refer to model), were recording meteorological information during the campaign (Fig. 2). The height of the station was 22 meters above sea level. R/V *Lance* was sailing during this period and its route was located in the Fram Strait within $100\,\mathrm{km}$ west and north of the position of satellite scenes. During the week of data collection, the weather conditions were varying and the temperature was fluctuating around 0°C We have no recorded information about the amount of precipitation during the campaign, but the cruise report describes long periods with fog until 2 September. To investigate how the distance between R/V Lance and the position of the satellite scenes influenced the meteorological information, 2 meter air temperature and surface pressure were extracted from the European Center for Medium-Range Weather Forecasts (ECMWF) re-analysis (ERA-interim; Dee et al., 2011). The parameters were extracted in 6-hours increments for both the position of R/V Lance and the satellite scenes (79.25°N 14.25°W). There was good agreement between ERA-interim air temperature and surface pressure at the two locations (Fig. 2). The re-analysis seems to overestimate the air temperature during the start of the campaign.

2.3 Study design

In the following subsections, the design of our study is presented.

2.3.1 Regions of interest

The area covered by the satellite scenes consists of sea ice with different geophysical properties. Some regions were homogeneous and some contained mixtures of different sea ice types. To simplify our study we focus on five different sea ice regions, representing the most typical sea ice types in the scenes (Fig. 3). The regions of interest were chosen to be as homogeneous as possible, and to represent five distinctly different sea ice types. All ROIs are situated along the helicopter flight track and are $400\,\mathrm{m}$ (along track) $\times$ $200\,\mathrm{m}$ (across track) in size. The selection of the ROIs was performed manually, based on color coded polarimetric images (Pauli and composite-representations) of the satellite scenes together with photos, sea ice thickness, surface roughness and melt pond fraction retrieved from the helicopter overflight. Example photos from each ROI are presented in Fig. 4 and sea ice thickness histograms for each ROI can be found in Fig. 5. Table 2 presents helicopter measurements for each ROI, including mean and modal sea ice thickness, mean melt pond fraction, surface roughness, and sea ice class labels according to WMO sea ice nomenclature (World Meteorological

Organisation, 1989). ROI1 represents an area with level medium thick FYI, found in the upper left part of the scene in Fig. 3. The sea ice in ROI1 was relatively smooth and had a moderate melt pond fraction. ROI2 represents the area of level thin FYI located in the middle of the scene. The sea ice in ROI2 was smooth with a high melt pond fraction. ROI3 and ROI4 represent areas of weathered deformed old ice, situated in the lower middle part of the scene. ROI3 represents thinner ice with a higher melt pond fraction than ROI4. ROI5 represents heavily deformed old ice, located in the lower part of the scene. Note that other areas of deformed ice can be seen as light-coloured regions in the right part of the scene possibly forming a shear ridge.

2.3.2 Polarimetric SAR features

Polarimetric SAR features combine information from the channels of a multi-polarisation SAR system, and they represent information about the scattering properties of the surface. The features studied were previously successfully used in segmentation of a wintertime sea ice scene (Moen et al., 2013). An overview of the features and their definitions is presented in Table 3. The features consist of relative kurtosis (RK), geometric brightness (B), cross-polarisation ratio ($R_{\mathrm{VH/VV}}$), co-polarisation ratio ($R_{\mathrm{VV/HH}}$), co-polarisation correlation magnitude ($|\rho|$) and co-polarisation correlation angle ($\angle\rho$). $R_{\mathrm{VH/VV}}$ is used instead of $R_{\mathrm{HV/HH}}$ as T2 has the polarisation combination VH$-$VV. By inspection, these two features show similar values in our dataset. $\angle\rho$ is equivalent to the more frequently used term co-polarisation phase difference ($\phi_{\mathrm{HH-VV}}$).

A full-polarimetric SAR system is transmitting and receiving both horizontal (H) and vertical (V) polarised electromagnetic waves, resulting in $d = 4$ possible polarimetric channels (S_{HH}, S_{HV}, S_{VH} and S_{VV}). Assuming reciprocity ($S_{\mathrm{HV}} = S_{\mathrm{VH}}$), the Lexicographic feature vector, $\boldsymbol{s}$, is given by equation

$$\boldsymbol{s} = \begin{bmatrix} S_{\mathrm{HH}} & \sqrt{2}S_{\mathrm{VH}} & S_{\mathrm{VV}} \end{bmatrix}^{\mathrm{T}}, \tag{2}$$

where T denotes transpose (Lee and Pottier, 2009). The covariance matrix, $\mathbf{C}$, is defined as the mean outer product of the Lexiographic feature vector

$$\mathbf{C} = \frac{1}{L}\sum_{i=1}^{L} \boldsymbol{s}_i \boldsymbol{s}_i^{*\mathrm{T}}, \tag{3}$$

where $\boldsymbol{s}_i$ is the single look complex vector corresponding to pixel i, L is the number of scattering vectors in a local neighbourhood and $*\mathrm{T}$ denotes the Hermitian transpose (Lee and Pottier, 2009). Hence, $\mathbf{C}$ can be written as

$$\mathbf{C} = \begin{bmatrix} \langle S_{\mathrm{HH}} S_{\mathrm{HH}}^* \rangle & \langle S_{\mathrm{HH}} S_{\mathrm{VH}}^* \rangle & \langle S_{\mathrm{HH}} S_{\mathrm{VV}}^* \rangle \\ \langle S_{\mathrm{VH}} S_{\mathrm{HH}}^* \rangle & \langle S_{\mathrm{VH}} S_{\mathrm{VH}}^* \rangle & \langle S_{\mathrm{VH}} S_{\mathrm{VV}}^* \rangle \\ \langle S_{\mathrm{VV}} S_{\mathrm{HH}}^* \rangle & \langle S_{\mathrm{VV}} S_{\mathrm{VH}}^* \rangle & \langle S_{\mathrm{VV}} S_{\mathrm{VV}}^* \rangle \end{bmatrix}, \tag{4}$$

where the $\langle \cdot \rangle$ is the sample mean over L scattering vectors and * denotes the complex conjugate.

The TS-X scenes included in our study are dual-polarimetric. The covariance matrix then reduces to a 2×2 matrix. This implies that the full feature set of six features could not be achieved for these scenes since the achievable feature set depends on the scenes' polarimetric channel combination (see Table 3). Note that RK and B in the TS-X scenes are calculated from reduced covariance matrices, and should not be directly compared to the similar RS-2 features.

$R_{\mathrm{VH/VV}}$, $R_{\mathrm{VV/HH}}$, $|\rho|$ and $\angle\rho$ are well known polarimetric features in sea ice applications (Drinkwater et al., 1992), while RK and B have seen less attention in the literature. RK is a measure of non-Gaussianity, and is defined as Mardia's multivariate kurtosis of a sample divided by the expected multivariate kurtosis of a complex normal distribution ($d(d+1)$) (Mardia, 1970; Doulgeris and Eltoft, 2010). $RK < 1$ points towards a distribution with broader shoulders and lighter tails than for Gaussian data, while $RK > 1$ implies a sharp peak close to the mean, and heavy tails relative to Gaussian distribution (DeCarlo, 1997). Large values of RK are expected for deformed sea ice due to scattering from a few strong reflections, and for inhomogeneous areas due to differences in intensity mixtures (Moen et al., 2013). B represents the intensity of the multichannel radar backscatter. It is closely related to the more familiar feature SPAN, i.e. trace($\mathbf{C}$), as they both represent the eigenvalues of the covariance matrix. B is however more sensitive to the smaller eigenvalues. $R_{VH/VV}$ is known as a measure of depolarisation (Drinkwater et al., 1992). In microwave scattering of sea ice, depolarisation is expected related to multiple scattering within the sea ice volume or to surface roughness (Scharien et al., 2012; Moen et al., 2013). $R_{VV/HH}$ is only dependent on the relative permittivity for very smooth surfaces within the Brag regime (Hajnsek et al., 2003). For rougher surfaces, the feature is expected to increase with incidence angle and relative permittivity, and decrease with increasing surface roughness (Drinkwater et al., 1991; Fung, 1994). With volume scattering, $R_{VV/HH}$ (dB) tends toward zero (Scharien et al., 2012). $|\rho|$ is a measure of the proportion of polarised backscatter, reaching unity when the co-polarisation channels are perfectly correlated (Drinkwater et al., 1992). The feature is expected to decrease with incidence angle, at an increasing rate for high salinity ice (Drinkwater et al., 1992; Gill et al., 2012). $\angle\rho$ is the relative difference in phase between the co-polarisation channels, describing the sea ice scattering history (Drinkwater et al., 1992). The feature depends on both the sea ice relative permittivity and surface roughness.

2.3.3 Data analysis

In this study, the sea ice type discrimination ability is evaluated through a maximum a posteriori (MAP) supervised classifier, using Bayes' decision rule (Theodoridis and Koutroumbas, 2009). The classifier assigns pixel x to class ω_j if

$$P(\omega_j|x) > P(\omega_i|x) \quad \forall j \neq i, \tag{5}$$

where $P(\omega_j|x)$ is the probability of class ω_j given the feature value x. The probability density functions (PDFs) are estimated with a Parzen kernel density estimator, using a Gaussian kernel function (Theodoridis and Koutroumbas, 2009). The bandwidth used is a function of the number of points in the sample and their distribution, as described in Bowman and Azzalini (1997). The pixels in the five ROIs are used as training areas, and each of the satellite scenes are classified individually. As the ROIs investigated are small, resulting in small sample sizes, leave-one-out cross validation is used in training and testing the classifier. A 7×7 pixels neighbourhood, $L = 49$, is used in the classification and a stepping window with steps of 5×5 pixels is employed to reduce neighbourhood overlap. The resulting classification accuracies obtained for each individual feature are used to evaluate the discrimination abilities of the features in each of the five scenes.

The temporal consistency of the individual features is studied qualitatively for the three RS-2 scenes, by inspecting the mean ROI values of each feature. We consider a feature temporally consistent if the ranking of the mean ROI values of the feature is similar in all three scenes. E.g., the ROI with the highest mean value for a specific feature has the highest mean value of that feature in all the three investigated scenes. Based on the result of temporal consistency, a reduced feature set of four features is suggested.

A feature-based automatic segmentation algorithm is tested on the five scenes in the dataset. It is tested both with the original full feature set, and with a reduced feature set excluding the most temporally inconsistent features. The segmentation uses multivariate Gaussian mixture models to model the features' PDF, and employs an expectation-maximization algorithm. Markov random fields are used for contextual smoothing. Further description of the segmentation approach is given in Doulgeris (2013) and Moen et al. (2013). A 21×21 pixels neighbourhood, $L = 441$, was used performing the segmentation. The size of the neigbourhood does not take into account the difference in resolution between the scenes, but assures an equal sample size in the extraction of the features. The algorithm was set to segment the scenes into six different segments. The number is chosen to allow for the five sea ice types described by the ROIs, in addition to one extra segment to allow for detection of other sea ice types and to assure some flexibility for the algorithm. For easier comparison, the area used in the segmentation is confined to the intersection of the individual scenes' geographical location (see the pink patch in Fig. 1). For each scene, the segmentation's performance is evaluated visually on its ability to separate the four main sea ice types represented in the ROIs (medium thick FYI, thin FYI, old ice and old deformed ice), and based on its ability to discriminate the pixels of the five ROIs into different segments.

3 Results

This section consists of three parts. The first two parts examine the individual sea ice type discrimination ability and the temporal consistency of six polarimetric SAR features. In the third part, an

automatic segmentation algorithm based on the investigated features is tested on the data set. Results for C- and X-band are presented separately, as differences in incidence angle, resolution and polarimetric channel combinations make a direct comparison inappropriate (see Table 1). The features in C-band are based on the full covariance matrix, while those in X-band are based on reduced covariance matrices as the TS-X scenes are dual polarisation scenes (see Table 3). Note that ROI5 is only present in the RS-2 scenes.

3.1 Individual features discrimination ability

The polarimetric features' individual capacity of classifying the investigated ROIs into separate classes is presented in Tables 4 and 5, for RS-2 and TS-X respectively. The presented values represent the diagonal values of the confusion matrices, i.e., the percentage of true classification. The best result for each ROI is highlighted in bold. All pixels from the five ROIs were included in the classification, and the experiment was performed separately for each of the scenes included in the study. From the two tables we note that none of the features individually was able to classify all the five ROIs in a single scene with high accuracy. All features do however give satisfying classification results for some of the sea ice types represented by the ROIs, in some of the scenes. Hence, by combining the features, all features could add value to a feature-based sea ice type segmentation algorithm. The best feature for discriminating a given ROI varies from scene to scene. In all scenes except T1, ROI4 seems to be the most challenging to separate from the others. ROI4 consisted of old ice, as did ROI3. An overlap between the PDFs of these two ROIs could be a reason for the poor discrimination result.

The result of the MAP classification for C- and X-band does not show large differences. The best classification accuracies in the C-band scenes are slightly higher than those in the X-band scenes, indicating a larger discrimination potential in C-band. This difference is not necessarily a result of different frequencies. RK and B are calculated from a reduced covariance matrix in the X-band scenes, and therefore contain less information. The lower incidence angles and higher resolution of the TS-X scenes could also contribute to the observed differences.

3.2 Temporal consistency of features

The temporal evolution of the feature means from each ROI are displayed in Figs. 6 and 7 for RS-2 and TS-X, respectively. The variances of the features within each ROI are displayed as error bars equivalent to two standard deviations. Due to different polarisation channel combinations (see Table 1), different features are displayed for T1 and T2 in Fig. 7. This also limits a temporal investigation in X-band, and we will in the following focus on the results in C-band.

As weather conditions and incidence angles are different for the RS-2 scenes in the dataset (see Table1), the mean ROI values of the features are expected to vary between the scenes even if sea ice conditions would be the same or very similar. Hence, when searching for temporally consistent

features, we look at the evolution of the ranking of the mean ROI values of each feature. For instance, studying RK in Fig. 6, the mean value within each ROI varies between the scenes. However, the relative relationship between the different mean values is almost constant. The RK of ROI5 does for instance take values between 1.05 and 1.15, but the RK value is always highest in this ROI. The same between-ROI-consistency during the investigated period can also be found for B, $R_{\mathrm{VH/VV}}$ and $\angle\rho$ (Fig. 6). The relative relationship of the mean ROI value of $R_{\mathrm{VV/HH}}$ and $|\rho|$ changes from scene to scene, hence no temporal consistency can be observed.

T2 shows similar relationships between the mean ROI values of the features as the RS-2 scenes for all three features extracted (Figs. 6 and 7). The same between-ROI relationship cannot be found for T1. The error bars in the TS-X ROIs are in general larger than in the RS-2 ROIs, which may indicate poorer discrimination ability of the TS-X scenes.

A feature-based sea ice segmentation algorithm depends on features with good discrimination ability and temporal consistency to give consistent results during changing geophysical conditions. This is especially important in the Arctic, as in situ information is often not available. Excluding temporally inconsistent features could help achieve a temporally stable segmentation during changing conditions. We therefore suggest a reduced feature set, consisting of RK, B, $R_{VH/VV}$ and $\angle\rho$ for late summer sea ice segmentation. A reduction of features in the feature set could of course also imply loss of important information and hence degradation in the segmentation performance. The following subsection will further explore the use of a reduced feature set.

3.3 Segmentation

From Fig. 8, the segmentations of R1 and R2 look reasonable compared to the information from the helicopter flight, both for the full (right) and reduced (left) feature set. The different segments seem to be associated with distinct sea ice types. One can recognize the thin FYI ice area in the middle of the scenes (violet), the heavily deformed old ice areas in the diagonal bottom-left part of the scenes (blue and turquoise), and two different sea ice types north (medium thick FYI, orange) and south (old ice, yellow) of the middle region. The segmentation of R3 (Fig. 8e) has a more granular appearance, and the areas with medium thick FYI are confused with the areas consisting of old ice (yellow, orange, grey). The differences between the segmentations with full and reduced feature sets for the three RS-2 scenes are small, but the segmentation of R3 becomes slightly noisier with the reduced feature set.

Figure 9 displays which segments the pixels of each of the ROIs were assigned to in all three RS-2 scenes, both for the full (left) and the reduced (right) feature sets. In general, the segmentations with the full feature set give good distinction between the different ROIs included in this study. In particular, the thin FYI in ROI2 and the deformed old ice in ROI5 were separated with an accuracy above 71 % from the other ROIs in all three scenes. In R1 and R2, the segmentation was not able to separate ROI3 and ROI4 clearly (Fig. 9a and c). These ROIs both contain old ice, with different

thicknesses and melt pond fractions; hence, the ice types in the ROIs are quite similar. In R3, the medium thick FYI in ROI1 was segmented to three different segments. Reducing the feature set by excluding the temporally inconsistent features does not affect the results for R1 and R2 (Fig. 9b and d). In R3, it improves the separation of medium thick FYI in ROI1, and reduces the discrimination between the thin FYI in ROI2 and the old ice in ROI3 (Fig. 9f).

The segmentations of the two TS-X scenes, based on the achievable features limited by their polarisation channels (see Table 3), are presented to the left in Fig. 10. In addition, T1 was segmented with a reduced feature set presented to the right in the same figure. The segmentation of T1 with a full achievable feature set gives a poor and granular impression. The area of thin FYI in the middle of the scene was not discriminated from the rest of the scene, and the deformed sea ice areas in the bottom-left diagonal were not fully segmented (green). Also the segmentation of T2 gives a slightly granular impression, but the areas of thin FYI in the middle of the scene (violet), and the areas of deformed ice in the bottom-left diagonal (blue and turquoise) were well segmented. Reducing the feature set in the segmentation of T1 seems to improve the segmentation of the area with thin first-year ice in the middle of the scene (violet), but granular noise is still present.

Figure 11 displays which segments the pixels in each of the ROIs were assigned to in the segmentations of the two TS-X scenes. For T1, both for the full achievable (left) and the reduced (right) feature set. Fig. 11a confirms the poor impression of the segmentation of T1 with full achievable feature set, giving minimal discrimination between the four ROIs. In the segmented image of T2, the thin FYI in ROI2 is separated from the other ROIs, while the rest of the ROIs are confused. Reducing the feature set in the segmentation of T1 (Fig. 11b) does not improve the segmentation performance, even if the visual inspection of Fig. 10b suggested a slight improvement for the whole scene.

4 Discussion

Among the six investigated features, $R_{VV/HH}$ and $|\rho|$ were found to be temporally inconsistent during the study. The temporal inconsistency could have several reasons. These features might have a stronger sensitivity to sea ice relative permittivity than the others. As stated in the introduction, relative permittivity will vary largely with temperature during warm conditions (Vant, 1974; Barber et al., 1998), and small temperature differences between the scenes could cause large differences in relative permittivity. In Bragg-scattering theory, $R_{VV/HH}$ is only dependent on the relative permittivity of the surface for smooth surfaces (Fung, 1994). Another possible reason for the inconsistency of these two features is a stronger sensitivity to changes in incidence angles than for the rest of the features. The incidence angle of the three RS-2 scenes varies between 38 and 48 degrees (see Table 1). $|\rho|$ varies linearly with incidence angle, according to Fig. 6, but the same dependency cannot be seen for $R_{VV/HH}$. Gill et al. (2013) did a study on feature temporal consistency in C-band between a winter and a spring scene on FYI north of Canada. They found, similar to this study, that $\angle\rho$ showed

high consistency during changing temperature conditions. In contradiction to our findings, they also found $R_{VV/HH}$ to have high temporal consistency. RK and B were not included in their study. Different incidence angles, sea ice types, snow conditions and season may explain the differences in results.

Choice of features and their temporal consistency is not the only factor affecting the results of the segmentation algorithm. Differences in incidence angle and resolution between the scenes, changing meteorological conditions and choice of segmentation parameters do all affect the outcome of our study. The incidence angles in our study vary between 26° (T2) and 48° (R2). As the backscatter signature from a sea ice surface depends on incidence angle, this is expected to affect the results. Between the RS-2 scenes, the incidence angle variation is small with a 10° difference. From Fig. 6, the influence of the changing incidence angle is limited, except for $|\rho|$. The pronounced difference in incidence angle between the RS-2 and TS-X scenes could contribute to the poorer performance of the segmentation algorithm in X-band, but a larger number of scenes with overlapping incidence angle are needed to confirm this. To obtain equal sample sizes in our study, the same neighbourhood size was used in filtering all scenes even if the scene resolution differed. The scenes with highest resolution would therefore have smaller spatial filter sizes. This difference in scale possibly influences the signature of physical properties of the surface, like surface roughness variation. Filter sizes adjusted to the resolution were tested during our investigations, but this made little difference to the results.

During the week of data collection, the air temperature was varying around 0°C, introducing difficult conditions for sea ice information retrieval from SAR. The distance between the meteorological measurements retrieved from R/V Lance and the study site makes detailed analysis of SAR weather dependence difficult. Some general events observed in the meteorological data could however help explaining our results. Both T1 and R2 were acquired during a period with air temperatures close to or above 0°C, conditions that are on the limit of suitability for sea ice type discrimination by SAR. As reported by Scharien et al. (2010), moisture in the upper sea ice layer could mask out volume scattering and hence lower the backscatter contrast between different sea ice types. The difficult conditions could explain the poor segmentation performance of T1. However, R2 was acquired during similar meteorological conditions with good segmentation results. Lower frequency, higher incidence angle and extra information contained in the cross-pol channel (lacking for T1) could all have contributed to a better segmentation of R2. The segmentation of R3 was poorer than those of the two other RS-2 scenes. Prior to the acquisition of R3, a drop in temperature and relative humidity could have caused rime on the sea ice surface (Drinkwater, 1995) or draining and refreezing of freshwater in the upper layers of the sea ice (Scharien et al., 2010). Both processes could cause a lower contrast between different sea ice types, and hence hamper the segmentation results. A refreeze of the sea ice could however also result in the opposite, enhanced volume scattering could lead to increased sea ice type discrimination.

Choice of sliding window size and number of segments are important for the segmentation results. The use of window size of 21×21 pixels or larger showed the best results in our dataset. The size of the window was in our case a trade-off between resolution details (small window) and segmentation with little speckle and larger continuous regions (large window). The choice of window size will also determine which kind of information one can retrieve about the sea ice surface. If information about small-scale structure like ridges, melt ponds and small leads is important, this requires a small window. Larger window sizes could be more appropriate to gain information about, for instance, sea ice age or type. Choice of sensor restricts how high a resolution is possible to achieve, and high resolution is at present coupled to small swath width. The number of segments was set in advance, based on visual inspection of the scenes and information retrieved from the helicopter-borne measurements. Choosing too few segments could force different sea ice types into a common segment, while increasing the number of segments could split an ice type into several segments.

5 Conclusions

We examined the potential of sea ice segmentation by C- and X-band multi-polarisation SAR features during late summer in the Fram Strait. Firstly, the individual features sea ice type discrimination ability and their temporal consistency were investigated. Secondly, an automatic feature-based segmentation was tested.

The ability of the individual features to discriminate five sea ice types during changing temperature conditions was evaluated by a MAP supervised classifier, and by a qualitative study of the temporal consistency of the features. The classification results revealed a potential in all individual features for discriminating some of the sea ice types from each other, but none of the individual features could separate the total set of sea ice types in any of the scenes. Hence, a combination of the features has the potential of segmenting the different sea ice types included in our study. Temporal consistency was evaluated by studying the ability of the features to rank the mean value of the five sea ice types in the same order throughout the three RS-2 scenes. Relative kurtosis, geometric brightness, cross-polarisation ratio and co-polarisation correlation angle were found to give good temporal consistency during changing temperature conditions. These features were suggested as a reduced feature set. Co-polarisation ratio and co-polarisation correlation magnitude were found to be inconsistent through the period investigated. Possible reasons for the two features' inconsistency could be a higher sensitivity to changes in relative permittivity or incidence angles. Our study demonstrates some of the difficulties of sea ice discrimination at temperatures close to 0°C, and highlights that it is important to cautiously select features for consistent sea ice monitoring during late summer. However, our study shows as well that it is possible to retrieve valuable information from multi-polarisation SAR imagery, even under these difficult conditions.

An automatic feature-based segmentation algorithm was tested on the dataset and evaluated for its ability to discriminate the five investigated sea ice types. The segmentation was tested for a full feature set of six features and for a reduced feature set of the four features showing the best temporal consistency. The segmentation in general performed well on the three RS-2 scenes. It showed good temporal consistency between the scenes, both for the full and for the reduced feature set. However, reducing the feature set slightly degraded the segmentation performance for one scene. The segmentation succeeded in segmenting some of the sea ice types in one of the two TS-X scenes. In the other scene the segmentation performed poorly. The poor performance might be a result of air temperatures above 0°C combined with low incidence angle and polarimetric channel combination HH-VV. Reducing the feature set introduced a slight improvement in this poorest segmented scene. In total, the automatic feature-based segmentation algorithm demonstrates a potential of sea ice type discrimination during late summer, and our results indicate that an exclusion of temporally inconsistent features could improve the segmentation results in some cases. To confirm this, more scenes need to be investigated.

Both C- and X-band scenes were included in the study, but differences in incidence angle, resolution and number of polarisation channels made a direct comparison with respect to frequency inappropriate. One of the X-band scenes showed promising results regarding sea ice type discrimination, close to those achieved for the quad polarimetric RS-2 scenes, even though it was a dual polarimetric scene. However, investigations of more scenes with different incidence angle and polarisation combinations are necessary to assess the potential of X-band in sea ice discrimination.

Future studies should also focus on a better physical understanding of the relation between SAR polarimetric features and geophysical properties. This could improve the interpretation of the segmented sea ice scenes, and possibly lead to an automatic labeling of the segments, a classification. The suitability of other features in late summer sea ice segmentation should also be explored. Multi-polarisation SAR images offer good possibilities for sea ice segmentation, but due to their limited swath width they are not suitable for operational ice charting. The development of compact polarimetry modes on new satellite missions like, e.g. RISAT-1, PALSAR-2, and Radarsat Constellation Mission, and the new wide quad polarimetric mode in RS-2, could increase the amount of polarimetric information on larger swath widths, and the possibilities of late summer sea ice investigations in these modes should be investigated.

Acknowledgements. The authors thank the captain, crew and scientist from the Norwegian Polar Institute onboard R/V *Lance* in the Fram Strait 2011 for data collection. Thanks also to Justin Beckers at University of Alberta, Canada, for preprocessing the laser altimeter measurements. Radarsat-2 data are provided by NSC/KSAT under the Norwegian–Canadian Radarsat agreement 2011 and TerraSAR-X data are provided by InfoTerra. This project was supported financially by the project "Sea Ice in the Arctic Ocean, Technology and Systems of Agreements" ("Polhavet", subproject "CASPER") of the Fram Centre, and by the Centre for Ice, Climate and

Ecosystems and the longterm ocean and sea ice monitoring programme in the Fram Strait of the Norwegian Polar Institute. This project was also supported financially by Regional Differensiert Arbeidsgiveravgift (RDA) Troms County.

References

Barber, D. G., Yackel, J. J., Wolf, R. L., and Lumsden, W.: Estimating the thermodynamic state of snow covered sea ice using time series Synthetic Aperture Radar (SAR) data, in: International Society of Offshore and Polar Engineers Vol. III, The Eighth International Offshore and Polar Engineering Conference, 24–29 May 1998, Montreal, Canada, 50-541998.

Beckers, J. F., Renner, A. H. H., Spreen, G., Gerland, S., and Haas, C.: Sea-ice surface roughness estimates from airborne laser scanner and laser altimeter observations in Fram Strait and north of Svalbard, Ann. Glaciol., 56, 235–244, doi:10.3189/2015AoG69A717, 2015.

Bowman, A. W. and Azzalini, A.: Applied Smoothing Techniques for Data Analysis, Oxford University Press, New York, 1997.

Brath, M., Kern, S., and Stammer, D.: Sea ice classification during freeze-up conditions with multifrequency scatterometer data, IEEE T. Geosci. Remote, 51, 3336–3353, 2013.

Carlstrom, A. and Ulander, L.: C-band backscatter signatures of old sea ice in the central Arctic during freeze-up, IEEE T. Geosci. Remote, 31, 819–829, doi:10.1109/36.239904, 1993.

Dabboor, M. and Geldsetzer, T.: Towards sea ice classification using simulated RADARSAT Constellation Mission compact polarimetric SAR imagery, Remote Sens. Environ., 140, 189–195, doi:10.1016/j.rse.2013.08.035, 2014.

DeCarlo, L. T.: On the meaning and use of kurtosis, Psychol. Methods, 2, 292–307, doi:10.1037/1082-989X.2.3.292, 1997.

Dee, D. P.,Uppala, S. M., Simmons, A. J., Berrisford, P., Poli, P., Kobayashi, S., Andrae, U., Balmaseda, M. A., Balsamo, G., Bauer, P., Bechtold, P., Beljaars, A. C. M., van de Berg, L., Bidlot, J., Bormann, N., Delsol, C., Dragani, R., Fuentes, M., Geer, A. J., Haimberger, L., Healy, S. B., Hersbach, H., Hólm, E. V., Isaksen, L., Kållberg, P., Köhler, M., Matricardi, M., Mcnally, A. P., Monge-Sanz, B. M., Morcrette, J. J., Park, B. K., Peubey, C., de Rosnay, P., Tavolato, C., Thépaut, J. N., and Vitart, F.: The ERA-Interim reanalysis: Configuration and performance of the data assimilation system, Quarterly J. Royal Meteorological Society,137,553-597, doi:10.1002/qj.828, 2011.

Doulgeris, A. P.: A simple and extendable segmentation method for multi-polarsation SAR images, in: Proc. of PolInSAR 2013, 6th International Workshop on Science and Applications of SAR Polarimetry and Polarimetric Interferometry, 28 January–1 February 2013, Frascati, Italy, ESA SP-713, European Space Agency, Paris, 2013.

Doulgeris, A. P. and Eltoft, T.: Scale mixture of Gaussian modelling of polarimetric SAR data, EURASIP J. Adv. Sig. Pr., 2010, 1–13, doi:10.1155/2010/874592, 2010.

Drinkwater, M.: Airborne and satellite SAR investigations of sea–ice surface characteristics, in: Oceanographic Applications of Remote Sensing, CRC Press, Boca Raton, Florida, 339–357, 1995.

Drinkwater, M., Kwok, R., Rignot, E., Israelsson, H., Onstott, R. G., and Winebrenner, D. P.: Potential applications of polarimetry to the classification of sea ice, in: Microwave Remote Sensing of Sea Ice, edited by: Carsey, F. D., vol. 68, Geophysical Monograph Series, American Geophysical Union, Washington, DC, 419–430, doi:10.1029/GM068, 1992.

Drinkwater, M., Kwok, R., Winebrenner, D. P., and Rignot, E.: Multifrequency polarimetric synthetic aperture radar observations of sea ice, J. Geophys. Res., 96, 20679–20698, doi:10.1029/91JC01915, 1991.

Eriksson, L. E. B., Borena, K., Dierking, W., Berg, A., Santoro, M., Pemberton, P., Lindh, H., and Karlson, B.: Evaluation of new spaceborne SAR sensors for sea-ice monitoring in the Baltic Sea, Can. J. Remote Sens., 36, S56–S73, 2010.

Fung, A. K.: Microwave Scattering and Emission Models and their Applications, Artech House Inc., Norwood, MA, 1994.

Gill, J. P., and Yackel, J. J.: Evaluation of C-band SAR polarimetric parameters for discrimination of first-year sea ice types, Can. J. Remote Sens., 38, 306–323, doi:10.5589/m12-025, 2012.

Gill, J. P., Yackel, J. J., and Geldsetzer, T.: Analysis of consistency in first-year sea ice classification potential of C-band SAR polarimetric parameters, Can. J. Remote Sens., 39, 101–117, doi:10.5589/m13-016, 2013.

Gogineni, S. P., Moore, R. K., Grenfell, T. C., Barber, D. G., Digby, S., and Drinkwater, M.: The effects of freeze-up and melt processes on microwave signatures, in: Microwave Remote Sensing of Sea Ice, edited by: Carsey, F. D., vol. 68, American Geophysical Union, Washington, DC, 329–341, 1992.

Haas, C., Lobach, J., Hendricks, S., Rabenstein, L., and Pfaffling, A.: Helicopter-borne measurements of sea ice thickness, using a small and lightweight, digital EM system, J. Appl. Geophys., 67, 234–241, doi:10.1016/j.jappgeo.2008.05.005, 2009.

Hajnsek, I. and Pottier, E. and Cloude, S.R.: Inversion of surface parameters from polarimetric SAR, IEEE T. Geosci. Remote, 41, 727–744, doi:10.1109/TGRS.2003.810702, 2003.

Hibler, W. D.: Removal of aircraft altitude variation from laser profiles of the arctic ice pack, J. Geophys. Res., 77, 7190–7195, doi:10.1029/JC077i036p07190, 1972.

Hughes, N. E., Wilkinson, J. P., and Wadhams, P.: Multi-satellite sensor analysis of fast-ice development in the Norske Øer Ice Barrier, northeast Greenland, Ann. Glaciol., 52, 151–160, 2011, doi:10.3189/172756411795931633, 2011.

Isleifson, D., Langlois, A., Barber, D. G., and Shafai, L.: C-band scatterometer measurements of multiyear sea ice before fall freeze-up in the Canadian Arctic, IEEE T. Geosci. Remote, 47, 1651–1661, 2009.

Jeffries, M. O., Schwartz, K., and Li, S.: Arctic summer sea-ice SAR signatures, melt-season characteristics, and melt-pond fractions, Polar Rec., 33, 101–112, doi:10.1017/S003224740001442X, 1997.

Kwok, R., Cunningham, G. F., Wensnahan, M., Rigor, I., Zwally, H. J., and Yi, D.: Thinning and volume loss of the Arctic Ocean sea ice cover: 2003–2008, J. Geophys. Res., 114, C07005, doi:10.1029/2009JC005312, 2009.

Kwok, R.: Outflow of Arctic Ocean Sea Ice into the Greenland and Barents Seas: 1979-2007, J. Climate, 22, 2438–2457, doi:10.1175/2008JCLI2819.1, 2009.

Laxon, S. W., Giles, K. A., Ridout, A. L., Wingham, D. J., Willatt, R., Cullen, R., Kwok, R., Schweiger, A., Zhang, J., Haas, C., Hendricks, S., Krishfield, R., Kurtz, N., Farrell, S., and Davidson, M.: CryoSat-2 estimates of Arctic sea ice thickness and volume, Geophys. Res. Lett., 40, 732–737, doi:10.1002/grl.50193, 2013.

Lee, J. S. and Pottier, E.: Polarimetric radar imaging: from basics to applications, CRC Press, Boca Raton, Florida, 2009.

Mäkynen, M. and Hallikainen, M.: Investigation of C- and X-band backscattering signatures of Baltic Sea ice, Int. J. Remote Sens., 25, 37–41, doi:10.1080/01431160310001647697, 2004.

Mardia, K. V.: Measure of multivariate skewness and kurtosis with applications, Biometrica, 57, 519–530, 1970.

Matsuoka, T., Uratsuka, S., Satake, M., Kobayashi, T., Nadai, A., Umehara, T., Maeno, H., Wakabayashi, H., Nakamura, K., and Nishio, F.: CRL/NASDA airborne SAR (Pi-SAR) observations of sea ice in the Sea of Okhotsk, Ann. Glaciol., 33, 115–119, 2001.

Meier, W. N., Hovelsrud, G. K., van Oort, B. E., Key, J. R., Kovacs, K. M., Michel, C., Haas, C., Granskog, M. A., Gerland, S., Perovich, D. K., Makshtas, A., and Reist, J. D.: Arctic sea ice in transformation: a review of recent observed changes and impacts on biology and human activity, Rev. Geophys., 52, 185–217, doi:10.1002/2013RG000431, 2014.

Moen, M.-A. N., Doulgeris, A. P., Anfinsen, S. N., Renner, A. H. H., Hughes, N., Gerland, S., and Eltoft, T.: Comparison of feature based segmentation of full polarimetric SAR satellite sea ice images with manually drawn ice charts, The Cryosphere, 7, 1693–1705, doi:10.5194/tc-7-1693-2013, 2013.

Onstott, R. G.: SAR and scatterometer signatures of sea ice, in: Microwave Remote Sensing of Sea Ice, edited by: Carsey, F., vol. 68, American Geophysical Union, Washington, DC, 73–104, 1992.

Parkinson, C. L. and Comiso, J. C.: On the 2012 record low Arctic sea ice cover: combined impact of preconditioning and an August storm, Geophys. Res. Lett., 40, 1356–1361, doi:10.1002/grl.50349, 2013.

Raney, R. K.: Hybrid-polarity SAR architecture, IEEE T. Geosci. Remote, 45, 3397–3404, 2007.

Renner, A. H. H., Dumont, M., Beckers, J., Gerland, S., and Haas, C.: Improved characterisation of sea ice using simultaneous aerial photography and sea ice thickness measurements, Cold Reg. Sci. Technol., 92, 37–47, doi:10.1016/j.coldregions.2013.03.009, 2013.

Renner, A. H. H., Gerland, S., Haas, C., Spreen, G., Beckers, J. F., Hansen, E., Nicolaus, M., and Goodwin, H.: Evidence of Arctic sea ice thinning from direct observations, Geophys. Res. Lett., 2012, 1–8, doi:10.1002/2014GL060369, 2014.

Scharien, R. K., Geldsetzer, T., Barber, D. G., Yackel, J. J., and Langlois, A.: Physical, dielectric, and C band microwave scattering properties of first-year sea ice during advanced melt, J. Geophys. Res., 115, C12026, doi:10.1029/2010JC006257, 2010.

Scharien, R. K., Yackel, J. J., Barber, D. G., Asplin, M., Gupta, M., and Isleifson, D.: Geophysical controls on C band polarimetric backscatter from melt pond covered Arctic first-year sea ice: Assessment using high-resolution scatterometry, J. Geophys. Res., 117, C00G18, doi:10.1029/2011JC007353, 2012.

Scharien, R. K., Landy, J., and Barber, D. G.: First-year sea ice melt pond fraction estimation from dual-polarisation C-band SAR – Part 1: In situ observations, The Cryosphere, 8, 2147–2162, doi:10.5194/tc-8-2147-2014, 2014a.

Scharien, R. K., Hochheim, K., Landy, J., and Barber, D. G.: First-year sea ice melt pond fraction estimation from dual-polarisation C-band SAR – Part 2: Scaling in situ to Radarsat-2, The Cryosphere, 8, 2163–2176, doi:10.5194/tc-8-2163-2014, 2014b.

Stephenson, S. R., Smith, L. C., Brigham, L. W., and Agnew, J. A.: Projected 21st-century changes to Arctic marine access, Climatic Change, 118, 885–899, doi:10.1007/s10584-012-0685-0, 2013.

Stroeve, J. C., Markus, T., Boisvert, L., Miller, J., and Barrett, A.: Changes in Arctic melt season and implications for sea ice loss, Geophys. Res. Lett., 41, 1216–1225, doi:10.1002/2013GL058951, 2014.

Theodoridis, S. and Koutroumbas, K.: Pattern Recognition, Academic Press, London, 2009.

Vant, M. R.: Dielectric properties of fresh and sea ice at 10 and 35 GHz, J. Appl. Phys., 45, 4712, doi:10.1063/1.1663123, 1974.

Table 1. Overview of the data set.

Date	Time (UTC)	Scene ID	Satellite, mode and polarisation	Incidence angle	Pixel spacing (azimuth × slant range)
29 Aug 2011	17:41	R1	Radarsat-2, Fine Quad, HH,HV,VH,VV	38.2°	$5.0\,\mathrm{m} \times 5.0\,\mathrm{m}$
30 Aug 2011	18:23	T1	TerraSAR-X, StripMap, HH,VV	29.4°	$2.4\,\mathrm{m} \times 1.9\,\mathrm{m}$
31 Aug 2011	18:23	R2	Radarsat-2, Fine Quad, HH,HV,VH,VV	48.2°	$4.7\,\mathrm{m} \times 5.1\,\mathrm{m}$
3 Sep 2011	14:09	–	Helicopter fligth	–	–
4 Sep 2011	18:07	R3	Radarsat-2, Fine Quad, HH,HV,VH,VV	44.4°	$5.1\,\mathrm{m} \times 6.8\,\mathrm{m}$
5 Sep 2011	17:00	T2	TerraSAR-X, StripMap, VH,VV	25.9°	$2.3\,\mathrm{m} \times 2.1\,\mathrm{m}$

Table 2. Detailed information about the regions of interest (ROIs) from helicopter-borne measurments and the corresponding sea ice class labels (WMO nomenclatura).

ROI ID	Mean (modal) sea ice thickness	Mean melt pond fraction	Surface roughness, R_q	Sea ice class labels
ROI1	$1.3\ (1.2)\,\mathrm{m}$	$17\,\%$	$0.098\,\mathrm{m}$	Medium thick first-year ice
ROI2	$0.6\ (0.6)\,\mathrm{m}$	$38\,\%$	$0.062\,\mathrm{m}$	Thin first-year ice
ROI3	$2.1\ (2.0)\,\mathrm{m}$	$26\,\%$	$0.231\,\mathrm{m}$	Old ice
ROI4	$3.7\ (3.3)\,\mathrm{m}$	$11\,\%$	$0.204\,\mathrm{m}$	Old ice
ROI5	$11.7\ (8.9)\,\mathrm{m}$	$3\,\%$	$0.575\,\mathrm{m}$	Old ice

von Saldern, C., Haas, C., and Dierking, W.: Parameterization of Arctic sea-ice surface roughness for application in ice type classification, Ann. Glaciol., 44, 224–230, 2006.

Warner, K., Iacozza, J., Scharien, R., and Barber, D.: On the classification of melt season first-year and multi-year sea ice in the Beaufort Sea using Radarsat-2 data, Int. J. Remote Sens., 34, 3760–3774, doi:10.1080/01431161.2012.760855, 2013.

World Meteorological Organisation: Sea-ice nomenclature and interational system of sea ice symbols, Tech. rep., World Meteorological Organisation, Geneva, Switzerland, 1989.

Yackel, J. J. and Barber, D. G.: Melt ponds on sea ice in the Canadian Archipelago: 2. On the use of RADARSAT-1 synthetic aperture radar for geophysical inversion, J. Geophys. Res., 105, 22061, doi:10.1029/2000JC900076, 2000.

Table 3. Polarimetric SAR features included in the study.

Polarimetric feature	Definition	Extracted for scene
Relative kurtosis	$\mathrm{RK} = \frac{1}{L}\frac{1}{d(d+1)}\sum_{i=1}^{L}\left[\mathbf{s}_i^{*\mathrm{T}}\mathbf{C}^{-1}\mathbf{s}_i\right]^2$	All scenes
Geometric brightness	$B = \sqrt[d]{\det(\mathbf{C})}$	All scenes
Cross-polarisation ratio	$R_{\mathrm{VH/VV}} = \frac{\left\langle S_{\mathrm{VH}}S_{\mathrm{VH}}^*\right\rangle}{\left\langle S_{\mathrm{VV}}S_{\mathrm{VV}}^*\right\rangle}$	R1, R2, R3, T2
Co-polarisation ratio	$R_{\mathrm{VV/HH}} = \frac{\left\langle S_{\mathrm{VV}}S_{\mathrm{VV}}^*\right\rangle}{\left\langle S_{\mathrm{HH}}S_{\mathrm{HH}}^*\right\rangle}$	R1, R2, R3, T1
Co-polarisation correlation magnitude	$\lvert\rho\rvert = \left\lvert\frac{\left\langle S_{\mathrm{HH}}S_{\mathrm{VV}}^*\right\rangle}{\sqrt{\left\langle S_{\mathrm{HH}}S_{\mathrm{HH}}^*\right\rangle\left\langle S_{\mathrm{VV}}S_{\mathrm{VV}}^*\right\rangle}}\right\rvert$	R1, R2, R3, T1
Co-polarisation correlation angle	$\angle\rho = \angle\left(\left\langle S_{\mathrm{HH}}S_{\mathrm{VV}}^*\right\rangle\right)$	R1, R2, R3, T1

Table 4. Classification accuracy of individual polarimetric features in the three Radarsat-2 scenes derived from MAP classification. The best result for each ROI in each scene are highlighted in bold.

Scene ID	Feature	Sea ice type classification accuracy (%)				
		ROI1	ROI2	ROI3	ROI4	ROI5
R1	RK	5	22	42	0	64
	B	1	**69**	**71**	**10**	**78**
	$R_{\mathrm{VH/VV}}$	**23**	0	38	0	51
	$R_{\mathrm{VV/HH}}$	7	49	15	0	40
	$\lvert\rho\rvert$	0	41	31	5	46
	$\angle\rho$	0	30	70	0	41
R2	RK	41	28	0	7	8
	B	31	63	**75**	**32**	23
	$R_{\mathrm{VH/VV}}$	19	**87**	0	18	**44**
	$R_{\mathrm{VV/HH}}$	0	70	40	0	26
	$\lvert\rho\rvert$	**57**	0	0	0	34
	$\angle\rho$	5	11	19	27	**44**
R3	RK	0	20	**60**	40	55
	B	38	45	24	26	54
	$R_{\mathrm{VH/VV}}$	3	40	2	40	**74**
	$R_{\mathrm{VV/HH}}$	**61**	35	0	**41**	0
	$\lvert\rho\rvert$	31	**50**	6	2	58
	$\angle\rho$	14	0	0	23	51

Table 5. Classification accuracy of individual polarimetric features in the two TerraSAR-X scenes derived from MAP classification. The best result for each ROI in each scene is highlighted in bold.

Scene ID	Feature	Sea ice type classification accuracy (%)			
		ROI1	ROI2	ROI3	ROI4
T1	RK	35	3	**24**	17
	B	54	0	21	**60**
	$R_{\mathrm{VV/HH}}$	54	17	16	19
	$\lvert\rho\rvert$	51	**44**	0	19
	$\angle\rho$	**59**	12	22	18
T2	RK	**44**	0	32	6
	B	41	23	**59**	10
	$R_{\mathrm{VH/VV}}$	16	**61**	19	**23**

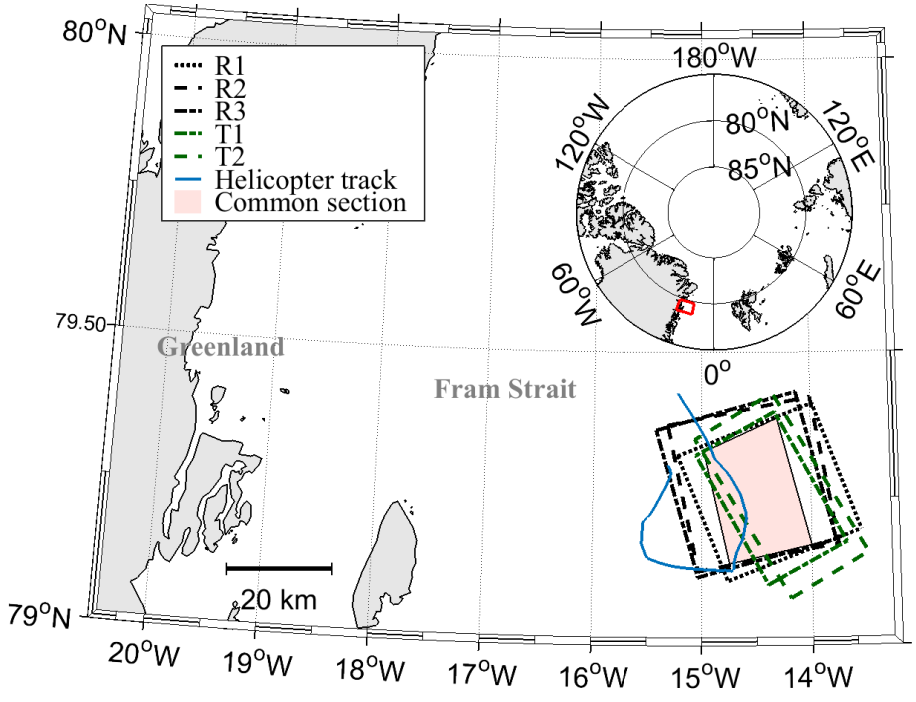

Figure 1. Map of the western Fram Strait showing the location of the satellite scenes included in the study and the track of the helicopter flight collecting airborne measurements for the study. The red box in the inset map of the Northern Hemisphere displays the geographical position of the area displayed. At the time of the flight, R/V *Lance* was slightly north of this map section.

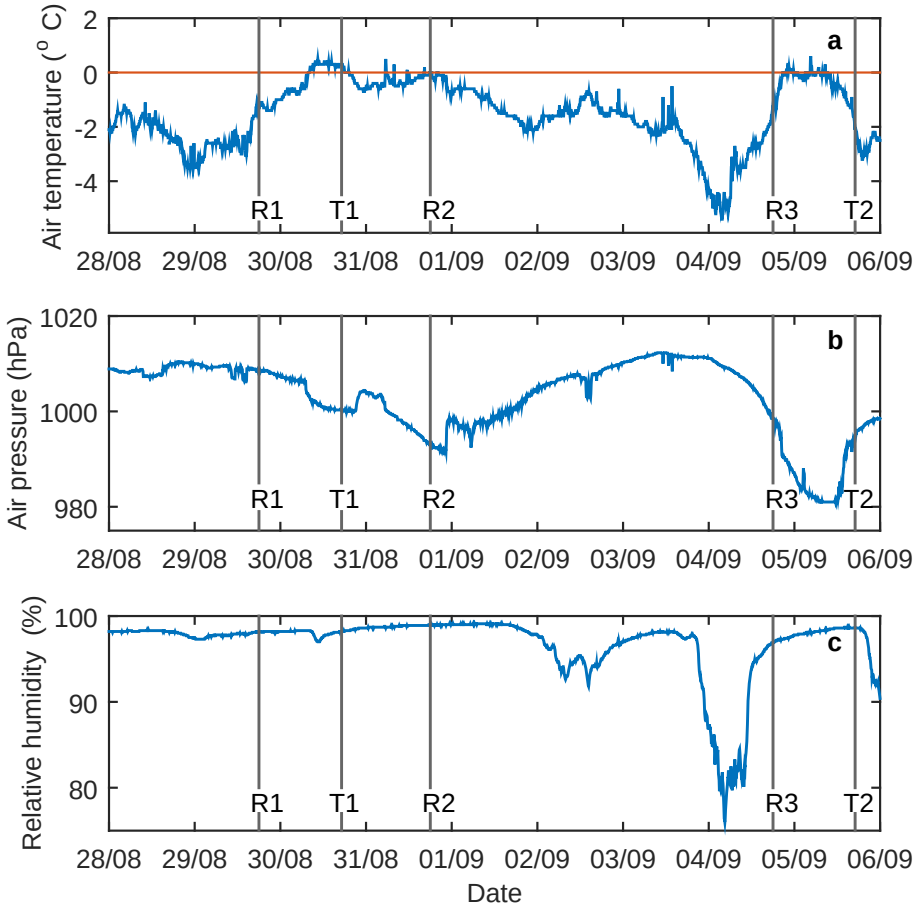

Figure 2. Air temperature **(a)**, air pressure **(b)** and relative humidity **(c)** during the campaign. The gray vertical lines represent the time of the acquisition of the satellite scenes.

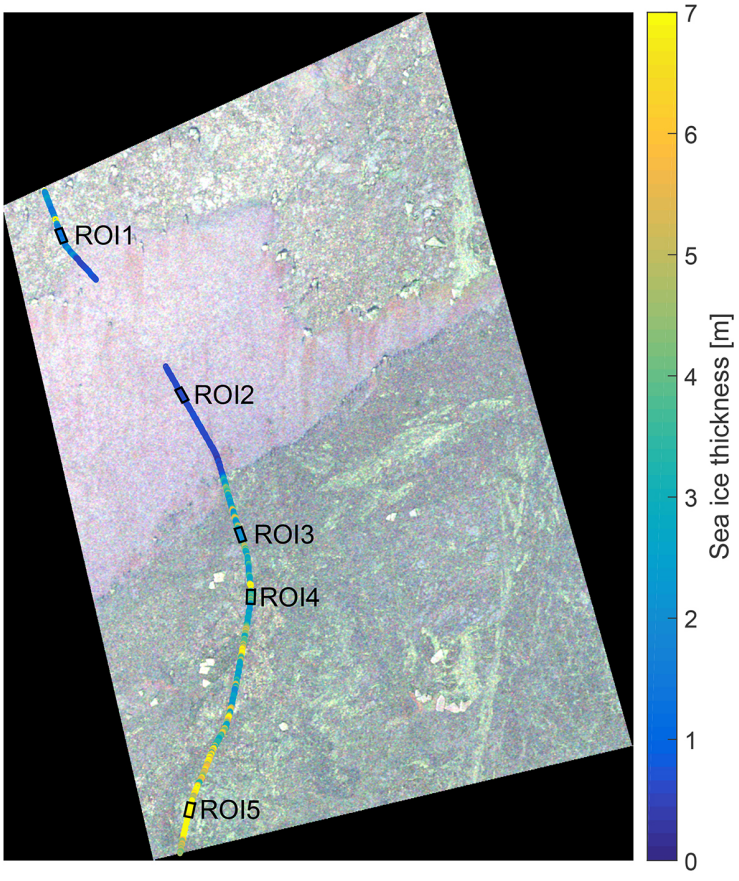

Figure 3. Position of regions of interest and helicopter thickness measurements displayed on the Radarsat-2 scene from 31 August 2011 (R2). The polarimetric image is a Pauli composite, the intensity channel combinations $|\mathrm{HH}-\mathrm{VV}|$, $2|\mathrm{HV}|$ and $|\mathrm{HH}+\mathrm{VV}|$ are assigned to the red, green and blue (RGB) channels, respectively.

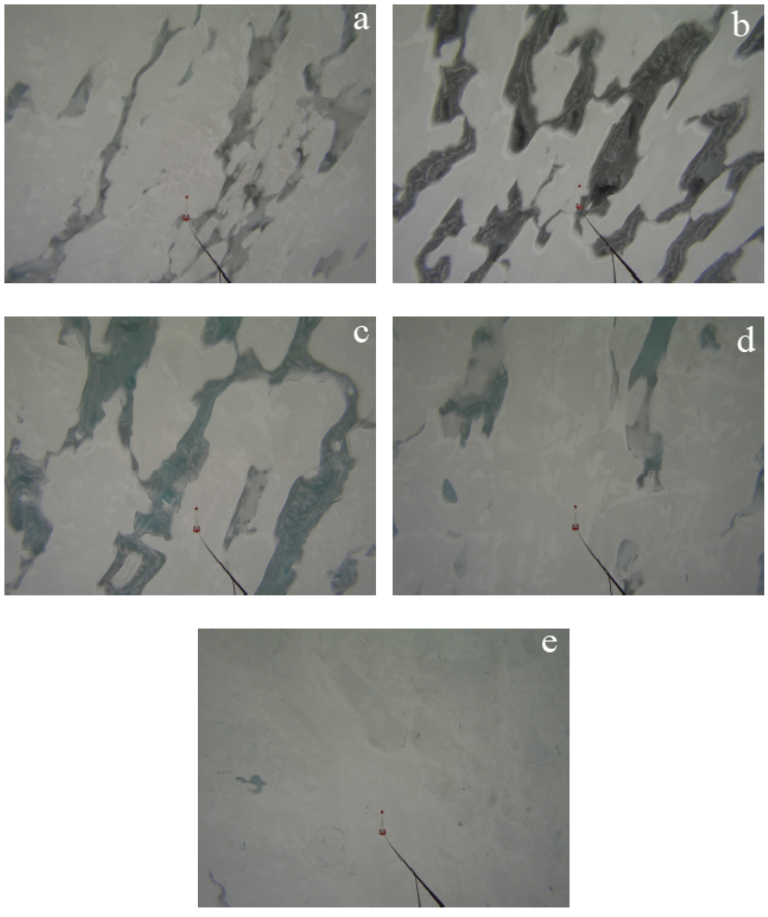

Figure 4. Example photos from the five regions of interest: **(a)** ROI1, **(b)** ROI2, **(c)** ROI3, **(d)** ROI4 and **(e)** ROI5. The photos are captured during the helicopter flight on 3 September 2011, and the EM-bird can be seen in the lower center part of each photo.

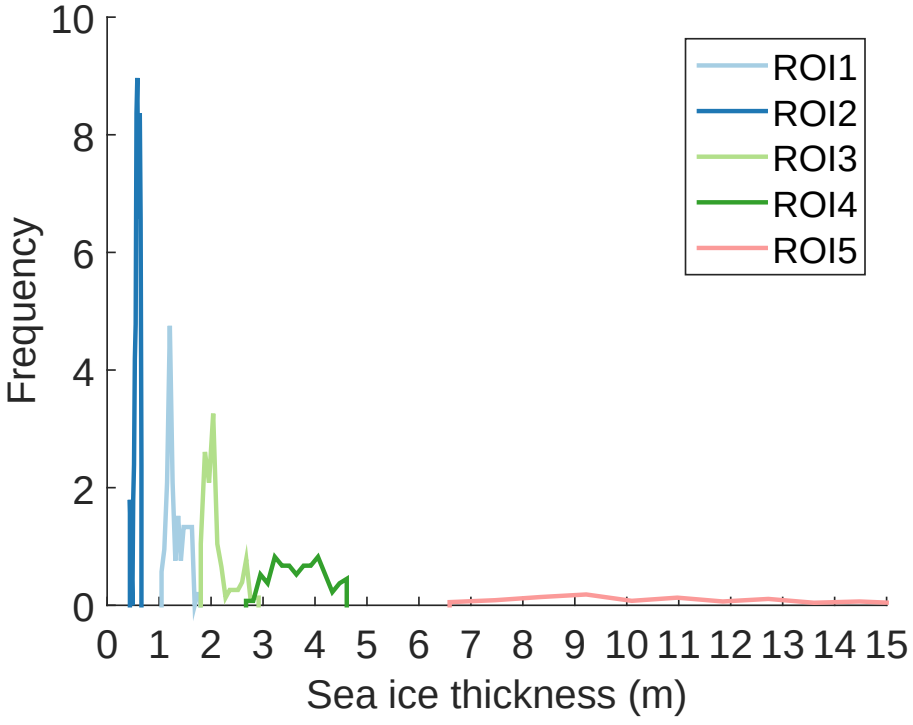

Figure 5. Histograms of sea ice thickness (m) measured during the helicopter flight 3 September 2011 for each of the five regions of interest (ROI).

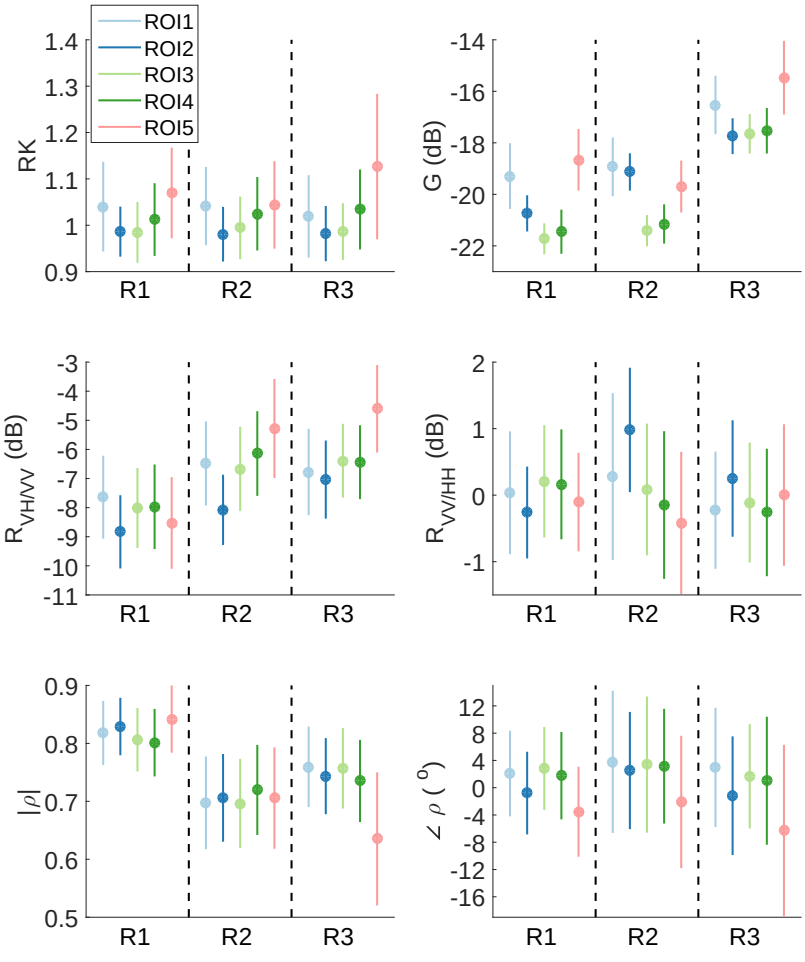

Figure 6. Mean values of the features in the regions of interest in the three Radarsat-2 scenes (R1, R2 and R3). The error bars are two standard deviations long.

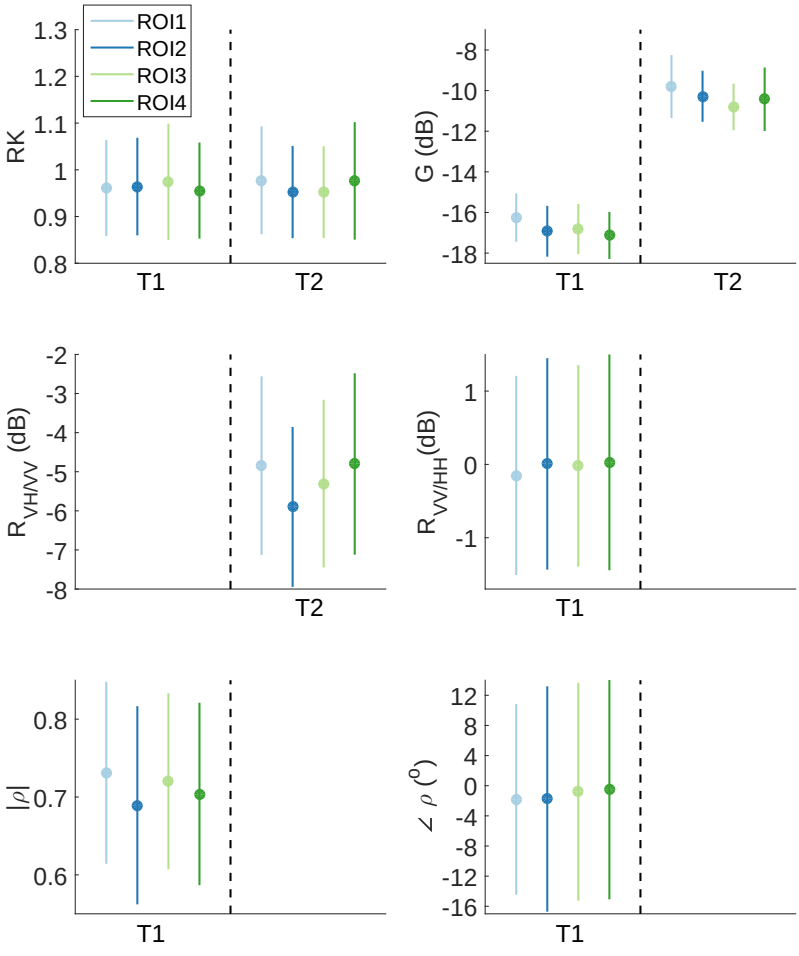

Figure 7. Mean values of the features in the regions of interest in the two TerraSAR-X scenes (T1 and T2). The error bars are two standard deviations long.

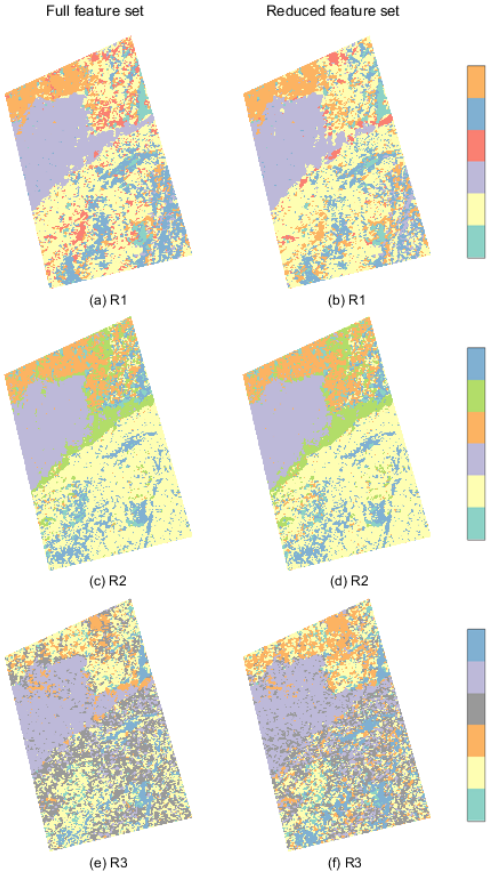

Figure 8. Segmentations of the three Radarsat-2 scenes (R1, R2 and R3) into six segments. To the left: segmentation with full feature set. To the right: segmentation with reduced feature set consisting of relative kurtosis, geometric brightness, cross-polarisation ratio and co-polarisation angle.

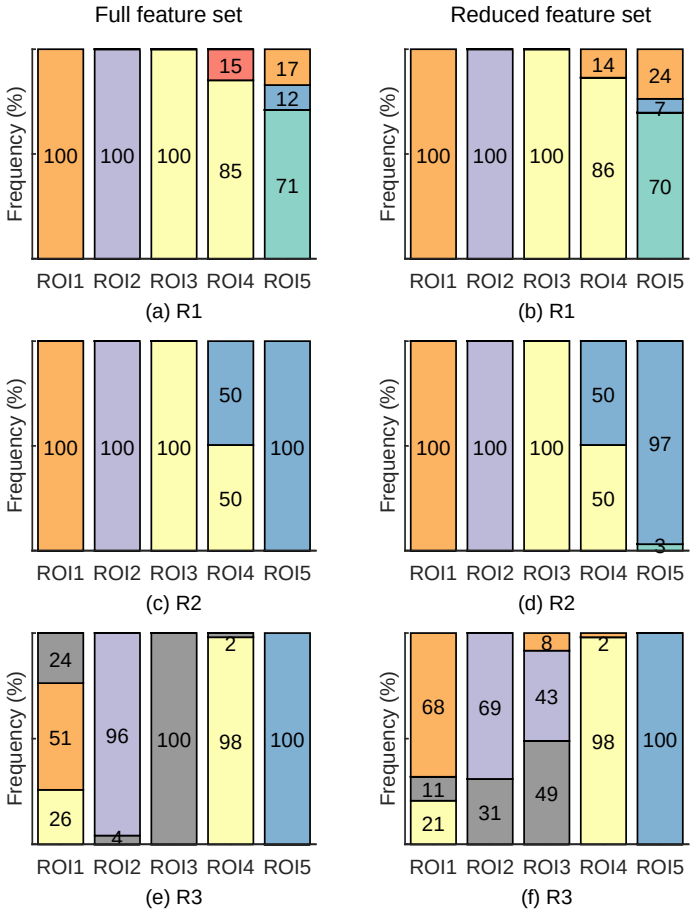

Figure 9. The segments assigned to the pixels in the five regions of interest by the segmentation of the three Radarsat-2 scenes (R1, R2 and R3). To the left: segmentation with full feature set. To the right: segmentation with reduced feature set.

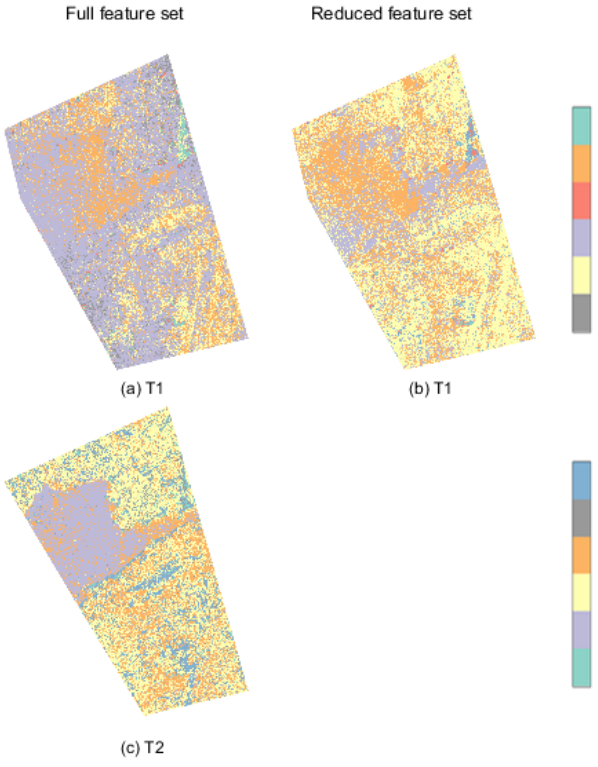

Figure 10. Segmentations of the two TerraSAR-X scenes (T1 and T2) into six segments. To the left: segmentation with full achievable feature set. For T1 the feature set consists of relative kurtosis, geometric brightness, co-polarisation ratio, co-polarisation correlation magnitude and co-polarisation correlation angle. For T2 the feature set consists of relative kurtosis, geometric brightness and cross-polarisation ratio. To the right: segmentation of T1 with the reduced feature set consisting of relative kurtosis, geometric brightness and co-polarisation correlation angle.

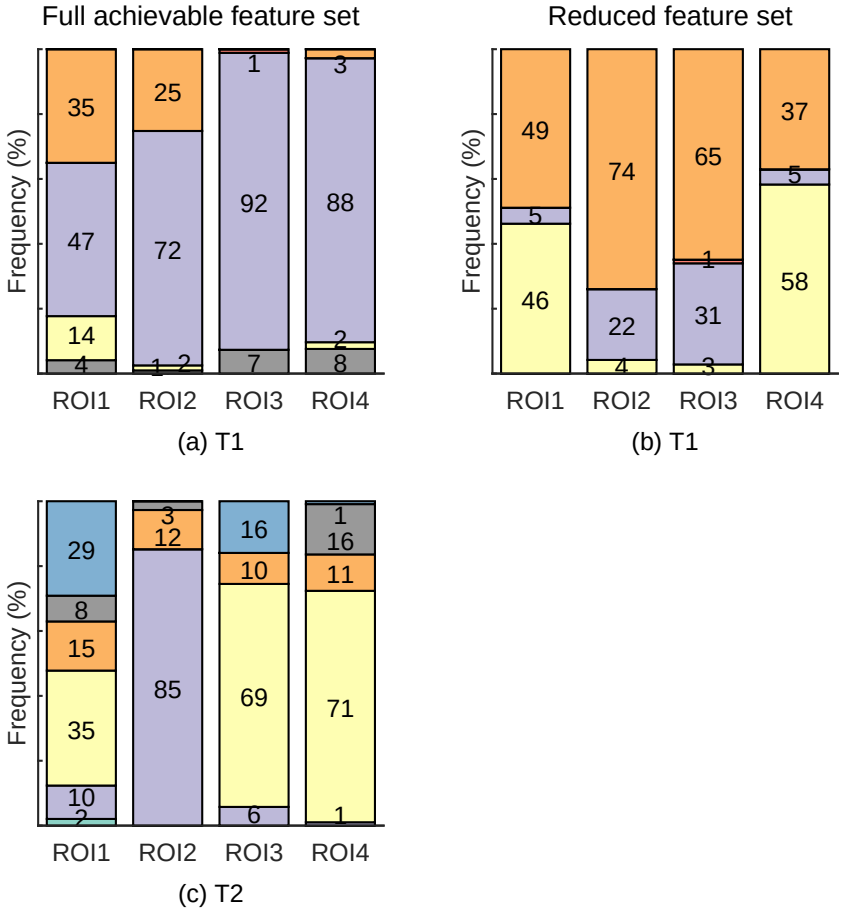

Figure 11. The segments assigned to the pixels in the four regions of interest by the segmentation of the two TerraSAR-X scenes (T1 and T2). To the left: segmentation of T1 and T2 with full achievable feature set. To the right: segmentation of T1 with reduced feature set.